



ELSEVIER

Available online at [www.sciencedirect.com](http://www.sciencedirect.com)

SCIENCE @ DIRECT®

Nuclear Instruments and Methods in Physics Research B 200 (2003) 397–405

**NIM B**  
Beam Interactions  
with Materials & Atoms

[www.elsevier.com/locate/nimb](http://www.elsevier.com/locate/nimb)

## Tomography studies of human foreskin fibroblasts on polymer yarns

Philipp Thurner<sup>a,b,\*</sup>, Bert Müller<sup>c</sup>, Felix Beckmann<sup>d</sup>, Timm Weitkamp<sup>e</sup>,  
Christoph Rau<sup>e</sup>, Ralph Müller<sup>b</sup>, Jeffrey A. Hubbell<sup>b</sup>, Urs Sennhauser<sup>a</sup>

<sup>a</sup> Swiss Federal Laboratories for Materials Testing and Research, Dübendorf CH-8900, Switzerland

<sup>b</sup> Institute for Biomedical Engineering, ETH and University Zürich, Zürich CH-8044, Switzerland

<sup>c</sup> Computer Vision Laboratory, ETH Zürich, Zürich CH-8092, Switzerland

<sup>d</sup> Hamburger Synchrotronstrahlungslabor HASYLAB at Deutsches Elektronen-Synchrotron DESY, Hamburg D-22607, Germany

<sup>e</sup> European Synchrotron Radiation Facility, Grenoble F-38043, France

### Abstract

Cell culture experiments are usually performed as in vitro studies based on 2D seeding and characterization (light microscopy). With respect to the in vivo situation, however, 2D studies are often inappropriate due to the 3D character of living tissue in nature. Textiles with their versatile 3D structures are chosen as suitable scaffolds in tissue engineering for 3D in vitro studies. Micro-computed tomography using X-rays ( $\mu$ CT) belongs to the most promising techniques for isotropic, noninvasive 3D characterization. Using synchrotron radiation (SR $\mu$ CT) the spatial resolution can be extended to the sub-micrometer range well below cell size.  $\mu$ CT does not need vacuum conditions making experiments in the hydrated state possible, as we show by data from SR $\mu$ CT acquired at second and third-generation synchrotron sources. We seeded human foreskin fibroblasts on polymer multifilament yarns. These composites, embedded in a hydrogel or fluid, are held in thin-walled glass capillaries. Since the composites consist of light elements, the cells have to be labeled for visualization by the use of highly absorptive agents, osmium and gold. In order to hold the label concentration as low as possible, we present a way to choose the photon energy for which the minimum concentration is reached. Differences in threshold selection for second- and third-generation synchrotron sources are pointed out, revealing the advantages of both types with respect to quantitative analysis. The study is based on appropriate staining methods and protocols developed in our laboratory. With the results we demonstrate that SR $\mu$ CT yields images similar to established electron and light microscopy but uncovers also the microstructure in 3D space.

© 2002 Published by Elsevier Science B.V.

**Keywords:** Computerized tomography; Synchrotron radiation; Cell complexes (geometry and topology); Image processing algorithms; Biological physics spectroscopic- and microscopic techniques

### 1. Introduction

Tissue engineering usually relies on 2D cell seeding and culturing. In many cases, however, such a 2D approach is not feasible. Since human tissue has almost exclusively 3D shape and structure, cell–cell

\* Corresponding author. Tel.: +41-1-632-4532.

E-mail address: [thurner@biomed.ee.ethz.ch](mailto:thurner@biomed.ee.ethz.ch) (P. Thurner).

contact in all three directions is important for its function, 3D scaffolds with more or less sophisticated 3D architectures are needed for cell culture experiments [1]. For the visualization of the individual cells within a 3D arrangement, conventional/confocal light or electron microscopy techniques are unsuitable, since the information in the third dimension is only accessible down to a maximal depth of about 0.5 mm. X-rays are the alternative probe to the visual light and electrons and can penetrate also through opaque objects. We hypothesize that X-ray techniques based on tomography are suitable tools for cell imaging, giving 3D information about their shape and distribution.

X-rays have been used for decades in medicine, especially for bone imaging. With the development of computed tomography (CT) by Hounsfield and McCormack [2] it became possible to retrieve 3D information of an investigated specimen, including the internal structure with high spatial resolution. In the following, CT was further improved with respect to spatial and density resolution as well as dose reduction. By the use of micro-focus bremsstrahlung sources the spatial resolution was extended down to about 10  $\mu\text{m}$  – termed micro-CT ( $\mu\text{CT}$ ). This resolution is limited due to the finite source size (of about several micrometers) and, even more important, limited flux, which is related to the acquisition time. Sources of smaller size and higher flux are available at synchrotron radiation facilities. Tomographic imaging applied at such institutions is termed synchrotron radiation  $\mu\text{CT}$  (SR $\mu\text{CT}$ ), whereas the spatial resolution for standard measurements is extended down to 1  $\mu\text{m}$  [3] or even better. Biological cells with typical dimensions between 5 and 10  $\mu\text{m}$  should be imageable using this technique. The other advantage of synchrotron radiation compared to bremsstrahlung sources is the high flux that allows selection of  $10^{-4}$  of the energy spectrum with feasible measuring time. This means that beam-hardening effects are avoided. The choice of the photon energy depends on the sample absorption related to the sample diameter and acquisition time. The photon energy is selected to minimize the acquisition time at sufficient signal to noise ratio [4] and according to the limitations of the beamline. For composites,

the contrast-yielding differences in absorption also depend on the selected photon energy. For cell cultures this is crucial, because the cells and the surrounding isotonic medium consist mainly of water and, therefore, exhibit almost no difference in absorption. Thus, cells in a hydrated environment are invisible per se, such that the cells have to be stained by highly absorptive contrast agents. Contrast agents with high atomic number, i.e. high X-ray absorption, are used in X-raying [5] and other techniques like scanning electron microscopy (SEM) [6] or magnetic resonance imaging (MRI) [7]. Suitable agents are osmium in the form of the post-fixative  $\text{OsO}_4$  and gold nanoparticles connected to lectins or antibodies that label features of interest on the cell membrane. In order to achieve sufficient contrast in the projections and further in the reconstructed tomogram the concentration of a contrast agent must reach a critical concentration that can be estimated using the equation of Grodzins [8],

$$f = \sqrt{\frac{B}{N_0 w^2 T} \frac{e^{\mu D/2}}{\mu w \sigma_c / \sigma}} \quad (1)$$

The minimally detectable atom fraction  $f$  at a given photon energy depends on the photon flux density  $N_0$ , the pixel length  $w$ , the total exposure time  $T$ , the average absorption coefficient  $\mu$ , the sample diameter  $D$ , the ratio of the absorption cross-sections of the contrast agent  $\sigma_c$  and the matrix  $\sigma$  and a factor  $B$  originating from the reconstruction algorithm, which is usually set to 2 [9]. These terms give the total number of photons that travel through the sample. In our case the parameter that can be varied for a given sample is the photon energy, influencing the ratio of absorption cross-sections and the average absorption coefficient of the sample. With the knowledge of photon flux, total exposure time, sample size and sample absorption properties as well as the voxel size, the minimum detectable atom fraction, expressed as the concentration in mol/l, can be plotted as a function of energy as shown in Fig. 1 for the two selected elements – Au and Os. The photon fluxes were estimated from values obtained at the beamlines BW2 (HASYLAB) [10] and ID22 (ESRF) [11] to be  $1.5 \times 10^{18}$  photons/ $\text{m}^2\text{s}$  and

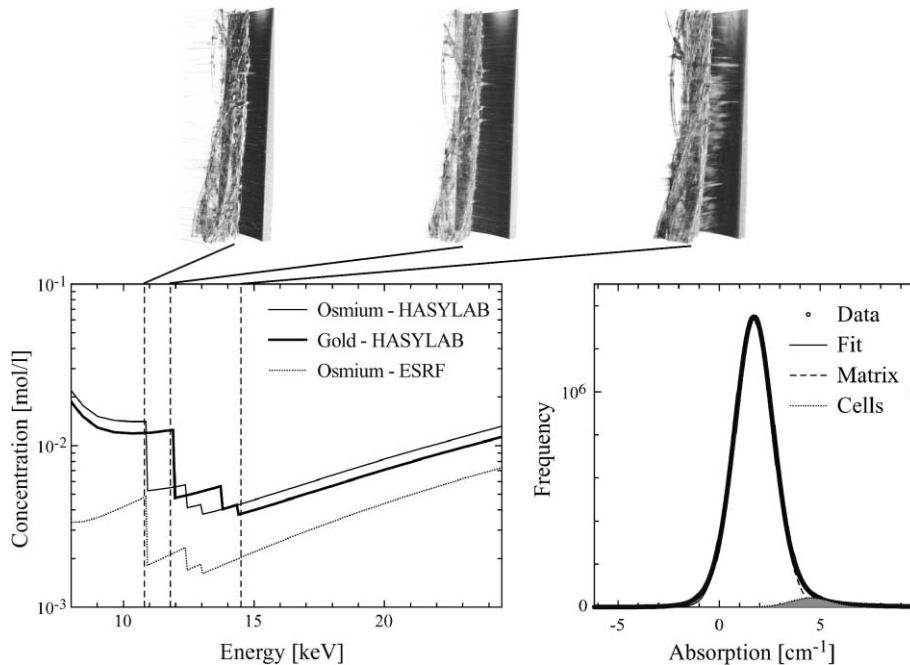


Fig. 1. Top: 3D renderings of the tomogram of a gold-enhanced sample (10 min development time), which was first stained with gold-labeled lectin from *Triticum Vulgaris* (concentration 1:10 in TBS, duration 3 h) and then post-fixed using  $\text{OsO}_4$  (concentration 2% in PBS, duration 2 h). Each measurement has been performed at selected photon energies of 10.8, 11.8 and 14.5 keV, as depicted by the straight lines. The spatial resolution corresponds to 3.5  $\mu\text{m}$ . Bottom left: Critical concentration for the detection of selected elements (osmium and gold) at the beamlines BW2 (HASYLAB) and ID22 (ESRF) in water, calculated after Grodzins [8]. The photon flux was assumed to be energy independent. Bottom right: Distribution of the absorption of the 1.48  $\mu\text{m}$ -wide voxels: two Gaussian functions representing the matrix and the stained cells respectively were fitted to the data. The fit was constraint assuming one half width for both peaks.

$1 \times 10^{20}$  photons/ $\text{m}^2$  s, respectively. They are assumed to be constant over the photon energy range used. For BW2 (HASYLAB) a sample diameter of 2 mm, a voxel size of 1.45  $\mu\text{m}$ , and a total exposure time of 3751 s were applied. For ID22 (ESRF) these values were 0.7 mm, 0.66  $\mu\text{m}$  and 3750 s, respectively. Absorption cross-sections for  $\text{H}_2\text{O}$ , Os and Au were calculated from their mass attenuation coefficients, which are accessible through the web-database of the National Institute of Standards (NIST) [12].

## 2. Methods

Human foreskin fibroblasts (HFF) have been seeded on poly-ethylene terephthalate (PET) multifilament yarns – 32 filaments with polygonal

shape and an outer diameter of about 20  $\mu\text{m}$  – as a model system. The yarns, pieces of 2–5 cm in length, were tied to knots at each end. Then they were cleaned in acetone, 70%-ethanol, and purified water in an ultrasonic bath for 30, 10 and 10 min, respectively. Subsequently, the yarns were dried in air overnight and plasma sterilized (Harrick Plasma Chamber PDC-32G) at an oxygen pressure of 0.5 mbar applying the power of 100 W for the period of 5 min. The  $\text{O}_2$  plasma not only sterilized the yarns but also enhanced their wetting properties, which is important for cell attachment and nutrient diffusion. The specimens were transferred into Dulbecco's modified Eagles medium containing 10% fetal bovine serum (FBS) and 1% broad-band antibiotic (ABAM) and put into a cell incubator at 37  $^\circ\text{C}$  and 5%  $\text{CO}_2$  for at least 5 h. Then the cell suspension was added for the seeding

process. The cell number was about  $10^5$  at seeding time and all specimens were put onto a 3D shaker installed in the cell incubator. After 1 or 2 days the samples were removed from the shaker and washed in sterile phosphate buffered saline (PBS), to remove damaged cells from the yarn surface. All yarns were fixated in 2.5% glutaraldehyde in PBS for 5 h after 3–4 days incubation time. The seeded yarns were then stained either with the post-fixative  $\text{OsO}_4$  in PBS or with gold-labeled lectin (*Triticum Vulgaris*, Sigma Product number L1894) in tristate buffered saline (TBS) or with both labels. The gold stain was further enhanced using a gold enhancement kit (Nanoprobes, Goldenhance–Lm/Blot) following the protocol given with the product. In the case of the combined gold-labeled lectin and  $\text{OsO}_4$  stain the samples were first incubated with the lectin, then the gold enhancement was performed prior to the application of the post-fixative  $\text{OsO}_4$ . A schematic for the different staining processes is given in Fig. 2. After staining, samples were washed in PBS twice. For tomographic imaging each specimen was transferred into a  $10\ \mu\text{m}$ -thin glass capillary,  $0.7\ \text{mm}$  in diameter, which was partially filled with PBS providing a hydrated sample environment. Then the

capillary was glued onto a sample holder using an epoxy resin and inserted in the tomography sample handler. The moderate thickness of the container is essential for the experiment since only a reasonably small fraction of the incoming radiation is absorbed in the thin glass wall. The photon energy was selected according to the calculated sensitivity curves shown in Fig. 1. It can be seen that the minimum concentration or highest sensitivity for gold is reached at  $14.5\ \text{keV}$ , which was used for scanning in most cases. The sharp edges in the concentration curves originate from absorption edges of the contrast-yielding element. Scanning just above and below such an edge can be done to extract the distribution of a single element [13]. After tomographic scanning the samples were checked by SEM imaging. For this purpose samples were dehydrated using 2,2-dimethoxy-propane and  $1\ \text{M}\ \text{HCl}$ . Then they were critical point dried using a Balzers CP030 device, a standard procedure in SEM preparation. After deposition of a  $5\ \text{nm}$ -thick chromium film by sputtering the samples were scanned at  $12\ \text{kV}$  electrons by means of a Hitachi S-900 SEM. All tomographic data-sets were reconstructed using a backprojection of filtered projections algorithm, the number of pro-

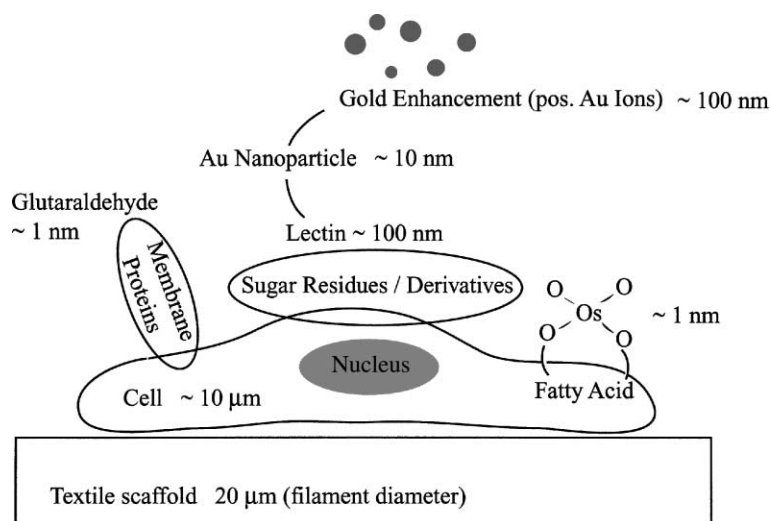


Fig. 2. Schematic of cell fixation and the staining processes used. The length scale of the different contrast agents is given for comparison. Glutaraldehyde fixates due to cross-linking of membrane proteins, osmium tetroxide binds to fatty acids (part of proteins). Lectins bind to sugar residues or derivatives on the cell membrane. In our case the lectin from *Triticum Vulgaris* is sensitive to *N*-acetyl- $\beta$ -D-glycosaminyl residues and *N*-acetyl- $\beta$ -D-glycosamine oligomers.

jections was set to 720 for the samples scanned at BW2 (HASYLAB) and 625 (yarn) and 1250 (yarn seeded with HFF cells) for the samples scanned at ID22 (ESRF), respectively.

### 3. Results and discussion

From the three 3D renderings in Fig. 1 it can be qualitatively seen that the element sensitivity curves are correct, the contrast for the cell material is best seen at the photon energy of 14.5 keV and decreases when the photon energy is reduced to 11.8 and 10.8 keV, respectively. The reason, why the yarn is still visible at the photon energy of 10.8 keV can be explained by the fact that the concentration of gold and osmium was estimated from the absorption behavior to be 0.14 and 0.15 mol/l, respectively, which is about one order of magnitude higher than the critical concentration according to Eq. (1) at this energy. The absorption values were obtained from the histogram, fitted with two Gaussians as shown in Fig. 1. The fit using the Levenberg–Marquardt algorithm was done with five parameters: center and amplitude for stained HFF-cells and matrix, respectively, and one full width at half maximum (FWHM) for both peaks. This is reasonable, because the concentra-

tion of the stain was low. Furthermore, the gold enhanced particles are estimated from SEM images to be about 100 nm in size, such that the probability of voxels partially filled with contrast agent and matrix is low and does not significantly influence the histogram broadening. The crossing point of the Gaussian curves, i.e.  $4.32 \text{ cm}^{-1}$  in Fig. 1, was used as the threshold for visualization [14]. Note, the negative values for the absorption are not real but the result of the final number of projections used for reconstruction.

The fact that the yarn starts to appear transparent at lower energies can be explained by the two different stains applied here: as the result of the much larger size of the lectin compared to  $\text{OsO}_4$  it is only effective on the yarn surface, and only this stain is further enhanced using the gold enhancement kit. Thus, we conclude that the concentration of osmium on cell membranes of cells inside the yarn is around the critical concentration of about 3–4 mmol/l.

The visibility of the individual filaments of the yarn in Figs. 1 and 4 is either due to the background of the used stains or the presence of extra cellular matrix (ECM), which may also contain to some extent staining material at its proteins and sugar derivatives. This explanation is further supported by the slice of the bare sample, measured at

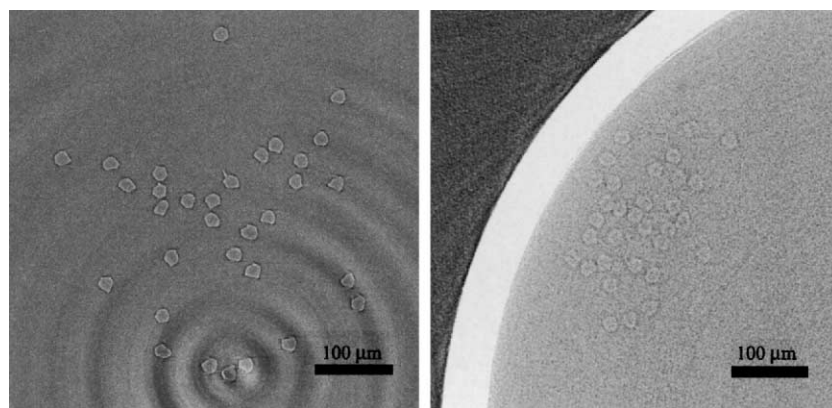


Fig. 3. Tomographic slices of a PET multifilament yarn (30 filaments each 20  $\mu\text{m}$  in diameter). Left: Yarn in dry environment scanned at ID22 (ESRF) using the photon energy of 20 keV. Right: Yarn seeded with HFF cells embedded in PBS, without a contrast agent, scanned at BW2 (HASYLAB) using the photon energy of 14.5 keV with the spatial resolution of 3.5  $\mu\text{m}$ . Due to edge enhancement originating from coherent radiation at the ESRF the yarn is visible in the left image although its absorption is almost identical to the surrounding air. Surprisingly we have found the same effect at a second-generation synchrotron radiation source as shown in the image on the right. Here, however, the effect is so small that it can be neglected for the quantitative analysis.

BW2 (HASYLAB) a second-generation synchrotron source, shown in Fig. 3 on the right hand side. The filaments are slightly visible, however, upon the presence of a higher absorbing agent they should disappear in the background noise. The case is different for beamline ID22 (ESRF), a third-generation synchrotron source, where edge enhancement is present due to highly coherent radiation [15]. This makes it possible to see the interfaces between the individual filaments and the surrounding air with the typical edge enhanced contrast ranging from very high to very low absorption values. The edge enhancement effect is

dependent on the distance between the sample and the detector, since the phase-shifted beams penetrating through the sample interfere with each other. For the measurement shown here this distance was chosen to be 8 mm, giving the beam enough space to form an interference pattern on top of the absorption contrast. Whether edge enhancement is desirable depends on the given imaging task and can be tuned for a special need. Edge enhancement makes it easier to visualize the interfaces. On the other hand, the exact position of the interfaces is difficult to determine. Furthermore, the edge enhancement influences the quantitative assessment

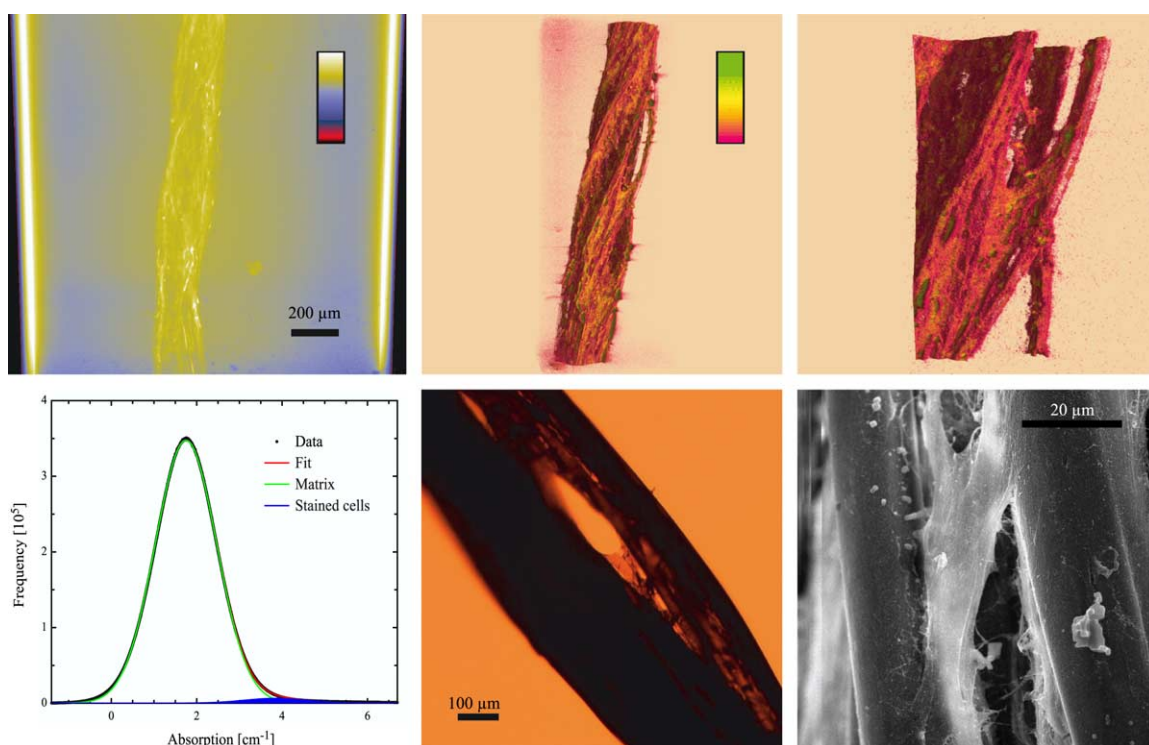


Fig. 4. Top left: Projection (absorption image) of a gold enhanced sample (5 min development time), which was stained with gold labeled lectin from *Triticum Vulgaris* (concentration 1:10 in TBS, duration 3 h). The color bar indicates the absorption values from low (black) to high (white). At each side the wall of the glass capillary is clearly visible, the stained cells on the yarn appear bright yellow to white in the center of the image. Data obtained at BW2 (HASYLAB) at the photon energy of 14.5 keV with the spatial resolution of 3.5  $\mu\text{m}$ . Top center: 3D rendering of the same sample, after selection of a cylindrical region of interest (ROI). For better visibility the image is false-colored according to the color bar ranging from low (red) to high absorption (green). Individual filaments of the yarn appear rather red due to residual contrast agent adsorbed on the PET-filaments. The cells themselves appear orange to green. Bottom left: Histogram of the cylindrical ROI (similar to that given in Fig. 1), fitted with two Gaussian functions – their crossing point at  $3.79\text{ cm}^{-1}$  is used as a threshold value for visualization. The detail of the 3D rendering (top right) shows close similarities to light (bottom center) and electron (bottom right) microscopy images. Consequently our approach to visualize cell cultures using SR $\mu$ CT is suitable. In addition the microstructure appears to be unchanged by the radiation on the micrometer scale as verified by the SEM image.

based on histogram analysis, i.e. the mean local absorption values. This makes it difficult to assess morphometric parameters such as cell volume or density, which will need uniform absorption throughout a given material in order to achieve solid binarization. In order to demonstrate the capability of SR $\mu$ CT as a tool for 3D imaging of cell cultures a measured tomogram of a sample is compared to images of the same/similar sample from SEM and LM, respectively (Fig. 4). The recorded projections obtained at the photon energy

of 14.5 keV with the spatial resolution of 3.5  $\mu\text{m}$  [16] show good contrast of the seeded yarn held in PBS. The reconstructed tomogram consisting of 1024 slices was 3D rendered using a threshold of 3.79  $\text{cm}^{-1}$  found by histogram analysis as described before. For better visibility the retrieved gray level image was false colored according to the color bar given in the inset. Although the difference in absorption between the filaments and the cells is small, it is possible to differentiate between the two materials. The filaments contain more

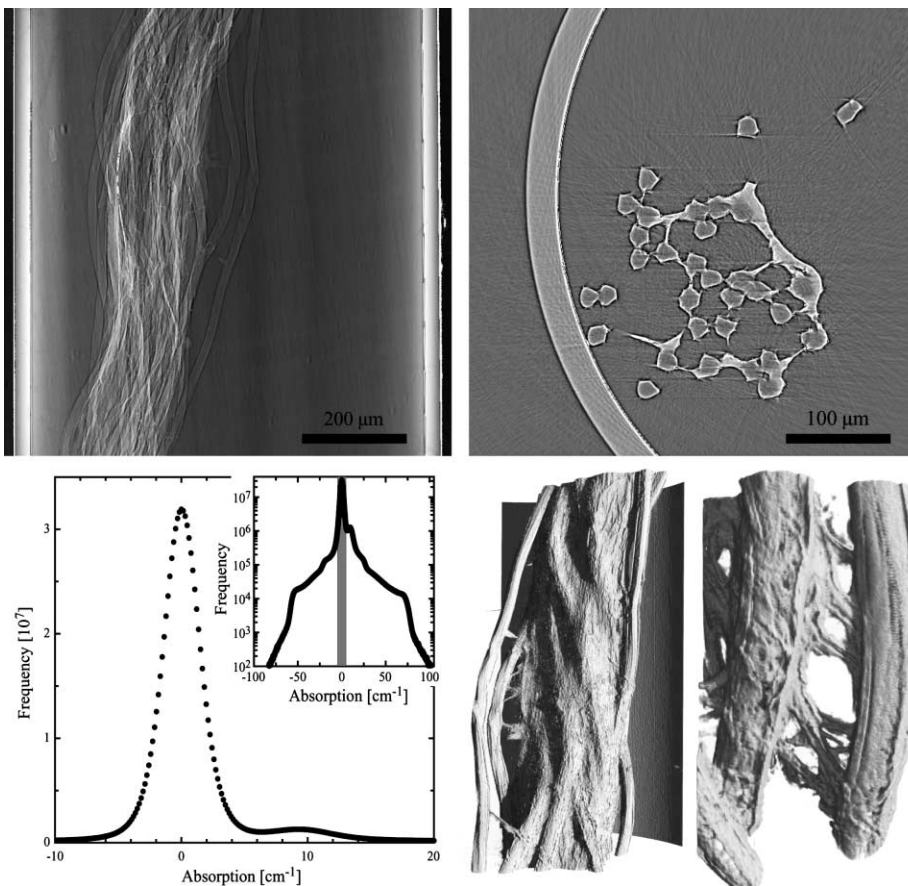


Fig. 5. Top left: Projection image of a sample post-fixed with  $\text{OsO}_4$  (concentration 0.3% in PBS, duration 2 h). The walls of the glass container and the yarn appear brighter than the environment (a fibrin hydrogel). The surfaces of the individual filaments and the HFF cells are highlighted due to edge enhancement. Data obtained at ID22 (ESRF) using the photon energy of 15 keV. Top right: Selected ROI of a reconstructed slice, interfaces between fibrin on one hand and filament and the cells on the other hand appears as an abrupt change in absorption. Bottom left: Histogram of the reconstructed data does not exhibit a Gaussian shape, which is even better seen in the inset where the same curve is given with logarithmic scale. The histogram is deformed due to the edge enhancement effect causing very high and very low absorption values. Thus segmentation has to be performed in a different manner: all voxels with absorption values in gray marked area are made transparent, uncovering the internal interfaces. Bottom right: 3D rendering of the thresholded tomogram and magnified detail.

red-colored voxels (lower absorption values) compared to the orange to green-colored voxels for the cells (higher absorption values). The magnified part of the 3D rendering looks very similar to the feature seen in Fig. 4 in the lower center: cells spread between individual filaments forming some kind of a rounded V-shape. The SEM image of the sample scanned using SR $\mu$ CT, given in Fig. 4, demonstrates not only the similarity of the observed structures, but also suggests that the potential radiation damages due to exposure to synchrotron radiation is not detectable in the microstructure. SEM and LM images of samples, which were not exposed to the synchrotron radiation, exhibit identical features. When comparing the experiments with gold and OsO<sub>4</sub>-stained cell cultures at the beamline BW2 (HASYLAB) and ID22 (ESRF) some differences come to light. In Fig. 5 a projection of the sample is shown exhibiting strong edge enhancement especially pronounced at the interfaces between the individual filaments and the matrix. The distance between sample and detector was 10 mm. There is, however, no enhancement at the interface between filaments and cells. It is assumed that the OsO<sub>4</sub> only penetrates the interface between cell and matrix but not the interface between cells and filaments the local absorption change from filament to cell would be rather small and consequently also the change in index of refraction. 3D rendering of the obtained data based on histogram analysis is not possible as a result of the pronounced edge enhancement. The effect is especially clear presenting the histogram on a logarithmic scale (Fig. 5, bottom right – inset). The extremely high and low values ranging between  $-100$  and  $100 \text{ cm}^{-1}$  due to the edge enhancement are surely not properties of the sample. Therefore, another procedure for 3D rendering is used: the histogram given in the inset in Fig. 5 shows a gray marked area around the matrix peak. All these values are made transparent (matrix) in the 3D rendering, and the structure of the HFF-cells seeded on the PET yarn is uncovered. The observed structures again look quite similar to images taken with the SEM and LM (cp. Fig. 4). The information, however, is mixed. The separation of individual cells and the yarn becomes extremely difficult.

#### 4. Conclusions

Since the uncovered structures are quite similar to images retrieved by techniques conventionally used for cell culture investigation, we conclude that SR $\mu$ CT is a suitable tool to investigate opaque, cell-seeded scaffolds with an internal structure such as pores in sponges. Histogram based gray level segmentation is not possible. The situation may change upon the application of image processing algorithms, which smoothen the images while conserving edges like anisotropic diffusion [17]. Surprisingly, this seems to be easier performed for the data obtained at a second-generation synchrotron source, since the edge enhancement is almost not present. This is only true, however, as long as it is impossible to include this extra phase information directly into the reconstruction algorithm. Alternatively, holographic tomography [18] may yield better results. Such an experiment is more complicated: three scans of the same sample at different distances to the detector have to be recorded. This means that the radiation dose is higher by a factor of three. The presented staining techniques and protocols work. The results from these first experiments can be improved. The lectin stain together with subsequent gold enhancement gives the best results so far, although cells inside the yarn are not stained due to the lectin size. This can be changed using an antibody of smaller size and applying gold enhancement. The enhancement of the OsO<sub>4</sub> stain is also possible using either the gold enhancement or the O–T–O technique [19]. Summarizing, it can be noted that the results are promising, although the goal to resolve individual cells in a hydrated state is not yet reached, which will most likely change by applying the mentioned improvements of the staining procedure and by the implementation of image processing algorithms.

#### Acknowledgements

The authors thank Martin Müller of ETH Zürich for SEM sample preparation. The authors gratefully acknowledge financial support from the Swiss National Science Foundation (2153-057127.99),

HASYLAB/DESY II-99-077: ‘Computed Microtomography’, and ESRF LS-1980: ‘3D Imaging of Biological Cells and Scaffolds using X-ray Microtomography’.

## References

- [1] M. Liu et al., *In Vitro Cell Dev. Biol. Anim.* 31 (1995) 858.
- [2] A.M. Cormack, *J. Appl. Phys.* 34 (1963).
- [3] U. Bonse, F. Busch, *Prog. Biophys. Molec. Biol.* 65 (1996) 133.
- [4] L. Grodzins, *Nucl. Instr. and Meth.* 206 (1983) 541.
- [5] H.N. Cardinal, D.W. Holdsworth, M. Drangova, B.B. Hobbs, A. Fenster, *Med. Phys.* 20 (1993).
- [6] L.G. Harris, I. ap Gwynn, R.G. Richards, *Scanning Microscopy* 13 (1999) 1.
- [7] P. Caravan, J.J. Ellison, T.J. McMurry, R.B. Lauffer, *Chem. Rev.* 99 (1999).
- [8] L. Grodzins, *Nucl. Instr. and Meth.* 206 (1983) 547.
- [9] D.A. Chesler, S.J. Riederer, N.J. Pelc, *J. Comp. Asst. Tomogr.* 1 (1977) 1.
- [10] [http://www-hasylab.desy.de/facility/experimental\\_stations/stations/BW2.htm](http://www-hasylab.desy.de/facility/experimental_stations/stations/BW2.htm).
- [11] [http://www.esrf.fr/exp\\_facilities/ID22/handbook.html](http://www.esrf.fr/exp_facilities/ID22/handbook.html) T. Weitkamp, C. Raven, A. Snigirev, in: U. Bonse (Ed.), *Developments in X-ray Tomography II*, Vol. 3772, SPIE, 1999, p. 311.
- [12] <http://physics.nist.gov/PhysRefData/XrayMassCoef/cover.html>.
- [13] U. Bonse et al., *Rev. Sci. Instr.* 60 (1989) 2478.
- [14] B. Müller, F. Beckmann, M. Huser, F.A. Maspero, G. Szekely, K. Ruffieux, P. Thurner, E. Wintermantel, *Biomol. Eng.* 19 (2002) 73.
- [15] A. Snigirev, I. Snigireva, V. Kohn, S. Kuznetsov, I. Schelokov, *Rev. Sci. Instr.* 66 (1995) 5486.
- [16] B. Müller, P. Thurner, F. Beckmann, T. Weitkamp, C. Rau, R. Bernhardt, E. Karamuk, L. Eckert, S. Buchloh, E. Wintermantel, D. Scharnweber, H. Worch, *Proc. SPIE* 4503 (2002) 178.
- [17] P. Perona, T. Shiota, J. Malik, *Anisotropic diffusion*, in: M.B. ter Haar Romeny (Ed.), *Geometry-Driven Diffusion in Computer Vision*, Kluwer Academic Publishers, Dordrecht, Boston, London, 1994, p. 73.
- [18] P. Cloetens, Ph.D. Thesis, Brussels, 1999.
- [19] A.M. Seligman, H.L. Wasserkrug, J.S. Hanker, *J. Cell. Biol.* 30 (1966).